Journal of
Marine Science and Engineering

MDPI

Article

Storm Surge Inundation Modulated by Typhoon Intensities and Tracks: Simulations Using the Regional Ocean Modeling System (ROMS)

Gangri Qin [1], Zhen Fang [1], Shuyu Zhao [2], Yanjiahui Meng [1], Weiwei Sun [1,3], Gang Yang [1,3], Lihua Wang [1,3] and Tian Feng [1,3,*]

1 Department of Geography & Spatial Information Techniques, Ningbo University, Ningbo 315211, China; 2011087073@nbu.edu.cn (G.Q.); 2111073005@nbu.edu.cn (Z.F.); 2211420015@nbu.edu.cn (Y.M.); sunweiwei@nbu.edu.cn (W.S.); yanggang@nbu.edu.cn (G.Y.); wanglihua1@nbu.edu.cn (L.W.)
2 Ningbo Meteorological Bureau, Ningbo 315012, China; zhaosy@ieecas.cn
3 Institute of East China Sea, Ningbo University, Ningbo 315211, China
* Correspondence: fengtian@nbu.edu.cn

Abstract: Storm surges are one of the most severe marine hazards, causing fatalities and devastating infrastructure. It is important to conduct research on storm surge hazards to achieve disaster avoidance and the protection of local populations. In this study, the Regional Ocean Modeling System (ROMS) was used to develop a framework to simulate the inundation (using the wet/dry method) of land in Ningbo, China during an extreme typhoon storm surge. The baseline simulation with the realistic typhoon intensity and track was well validated by meteorological and ocean tidal observations. Using reanalysis and an asymmetric typhoon wind field from the Holland model as atmospheric forcing, we presented different storm surge inundation scenarios regarding various intensities and tracks. The results revealed that typhoon storm surges are significantly affected by both the intensities and tracks of typhoons. Specifically, when Ningbo was located in the navigable semicircle, increasing the typhoon intensity not only resulted in the total inundation area of the whole study area from 108.57 km^2 to 139.97 km^2, but also led to significant negative storm surges in some sea areas. When Ningbo was exposed to the dangerous semicircle of the intensified typhoon, the storm surge along the coast of the Xiangshan Bay could exceed 4 m, amplifying the total inundation area to 245.41 km^2. Thus, it was evident that the location of the impacted region within the typhoon's wind field plays a critical role in determining the severity of the storm surge. These results provide valuable suggestions for storm surge disaster prevention and mitigation for local governments.

Keywords: ROMS; typhoon storm surges inundation; Holland model; Ningbo

check for updates

Citation: Qin, G.; Fang, Z.; Zhao, S.; Meng, Y.; Sun, W.; Yang, G.; Wang, L.; Feng, T. Storm Surge Inundation Modulated by Typhoon Intensities and Tracks: Simulations Using the Regional Ocean Modeling System (ROMS). *J. Mar. Sci. Eng.* **2023**, *11*, 1112. https://doi.org/10.3390/jmse11061112

Academic Editor: Efim Pelinovsky

Received: 21 April 2023
Revised: 21 May 2023
Accepted: 22 May 2023
Published: 24 May 2023

1. Introduction

There are many types of marine hazards such as huge waves, sea ice, red tides, tsunamis, and storm surges. Studies have shown that in some areas, storm surges can be more destructive and have a greater impact than earthquakes [1]. A storm surge is one of the most severe marine hazards, claiming lives and destroying property. A storm surge is defined as an abnormal change in sea level, associated with either an extratropical or tropical storm [2]. Storm surges are divided into positive and negative storm surges, according to the resulting sea level change [3]. If a storm surge occurs at the time of superposition with the astronomical high tide level, it will produce a significantly high water level. The huge waves caused by strong winds and heavy precipitation often result in a sudden rise in water levels in coastal areas, leading to the destruction of coastal defense buildings, local coastal flooding, scouring and erosion of coastal coasts, and significant economic losses and casualties [4].

Ningbo, one of China's major economic centers and one of the country's most vibrant and competitive cities, is located on the east coast of the country. The Ningbo-Zhoushan port has become the world's largest port, and its favorable sea, land, and air traffic conditions play crucial roles in China's economic development. However, Ningbo is also one of the most frequently and severely affected areas from typhoon storm surges in China [5]. Statistics reports that between 2016 and 2021, the city had been hit by 26 storm surge disasters, 20 of which were caused by typhoons, resulting in direct economic losses of approx. USD 268 million (The Ningbo Marine Disaster Bulletin [6]). Typhoon storm surges have threatened the lives of residents and caused significant economic losses to local enterprises and residents. Therefore, studying the impact of storm surges on Ningbo's coastal areas is of great theoretical and practical significance.

In the early days, the study of storm surges was mainly based on empirical observations of water level changes during typhoons [7]. With the development of computer technology in the 20th century, Hansen [8] used the Swedish electronic computer BESK to study storm surges in the North Sea in Europe. In the 1970s, Jelesnianski [9] conducted numerical simulations of storm surges by considering bottom friction, and proposed a storm surge prediction system SPLASH (Special Program to List Amplitude of Surges from Hurricanes). In 1984, Jelesnianski, et al. [10] developed a new two-dimensional numerical storm surge prediction model called SLOSH by improving the SPLASH model. With the advancement and improvement of storm surge numerical simulation, research on a three-dimensional storm surge numerical model has also been greatly promoted. Models such as ADCIRC [11], DELFT3D [12], POM [13], and FVCOM [14] have been widely used in this field. Weisberg and Zheng [15] utilized the finite-volume coastal ocean model (FVCOM) to investigate the responses of storm surges in the Tampa Bay to the hurricane landing location, direction, intensity, and movement speed. Cuadra, et al. [16] employed Delft3D-Flow to simulate the storm surge inundation process in the Bantayan region of the Philippines caused by Typhoon Haiyan, and obtained an inundation map to provide a basis for coastal disaster prevention. Jisan, et al. [17] employed the DELFT3D model to investigate the impact of sea level rise on storm surges and floods in coastal regions of Bangladesh.

Recent research on storm surges has been mostly based on FVCOM [18–20], ADCIRC [21–23], and other models that consider the situation of seawater inundating land during typhoons. In contrast, studies utilizing the ROMS model have placed greater emphasis on the changes in the water level and flow induced by storm surges but have paid less attention to the inundation of coastal regions by seawater [2,24–26]. This is primarily attributable to the ROMS land/sea mask remaining constant throughout the simulation, thereby precluding the ability to model the inundation. The ROMS model can integrate many different physical and ecological processes, such as marine biology, geochemistry, sedimentation, and ocean surface waves, to simulate various marine and coastal environmental conditions [27–29]. The versatility and scalability of the ROMS model make it an excellent tool for studying storm surge inundation, providing a wealth of possibilities and development space for future research in this area.

In this study, we used the ROMS wet/dry method to investigate the typhoon storm surge inundation process. Since the ROMS model lacks the function for constructing a typhoon wind field, we used the Holland wind field [30] to construct an asymmetric typhoon wind field model. This allowed us to use the ROMS model to study ocean changes and development under various typhoon events. The structure of this study is organized as follows. Section 2 introduces the ROMS model, the wet/dry method, the asymmetric typhoon wind field model, the model configuration, data, and experimental design. The comparison and analysis of modeling the experimental results are presented in Section 3. Section 4 draws the summary and conclusions.

2. Model and Method

2.1. Hydrodynamic Module

The Regional Ocean Model System (ROMS) is a numerical model used for simulating oceanic circulation, mainly developed by researchers at the University of California, Los Angeles (UCLA), Rutgers University, and the Institute of Research and Development (IRD) in France. The ROMS is a free-surface, terrain-following, three-dimensional primitive equation ocean model that considers processes such as sedimentation, ecology, and data assimilation [31,32]. The model uses vertically stretched terrain-following coordinates in the vertical direction, and a curvilinear Arakawa-C grid in the horizontal direction. Based on the hydrostatic and Boussinesq approximations, the ROMS uses the finite difference method to solve the three-dimensional Reynolds-averaged Navier–Stokes equations (RANS) of the free surface [31]. Its governing dynamical [32] equations, in Cartesian horizontal coordinates and the vertical stretched terrain-following coordinates, are as follows.

$$\begin{gathered}\frac{\partial(H_z u)}{\partial t}+\frac{\partial(uH_z u)}{\partial x}+\frac{\partial(vH_z u)}{\partial y}+\frac{\partial(\Omega H_z u)}{\partial \sigma}-fH_z v= \\ -\frac{H_z}{\rho_0}\frac{\partial p}{\partial x}-H_z g\frac{\partial \zeta}{\partial x}-\frac{\partial}{\partial \sigma}\left(\overline{u'w'}-\frac{\mathrm{v}}{H_z}\frac{\partial u}{\partial \sigma}\right)\end{gathered} \tag{1}$$

$$\begin{gathered}\frac{\partial(H_z v)}{\partial t}+\frac{\partial(uH_z v)}{\partial x}+\frac{\partial(vH_z v)}{\partial y}+\frac{\partial(\Omega H_z v)}{\partial \sigma}-fH_z u= \\ -\frac{H_z}{\rho_0}\frac{\partial p}{\partial y}-H_z g\frac{\partial \zeta}{\partial y}-\frac{\partial}{\partial \sigma}\left(\overline{v'w'}-\frac{\mathrm{v}}{H_z}\frac{\partial v}{\partial \sigma}\right)\end{gathered} \tag{2}$$

$$-\frac{1}{\rho_0}\frac{\partial p}{\partial \sigma}-\frac{g}{\rho_0}H_z\rho=0 \tag{3}$$

The continuity equation can be written as the following.

$$\frac{\partial \xi}{\partial t}+\frac{\partial(H_z u)}{\partial x}+\frac{\partial(H_z v)}{\partial y}+\frac{\partial(H_z \Omega)}{\partial \sigma}=0 \tag{4}$$

The scalar transport can be given by the following.

$$\frac{\partial(H_z C)}{\partial t}+\frac{\partial(uH_z C)}{\partial x}+\frac{\partial(vH_z C)}{\partial y}+\frac{\partial(\Omega H_z C)}{\partial \sigma}=-\frac{\partial}{\partial \sigma}\left(\overline{c'w'}-\frac{\mathrm{v}}{H_z}\frac{\partial C}{\partial s}\right)+C_{source} \tag{5}$$

The water state equation can be written as the following.

$$\rho=f(C,p) \tag{6}$$

where u, v, and Ω are the components of the velocity in the horizontal and vertical directions (terrain-following coordinates), respectively; ξ is the free-surface elevation which can be wave-averaged; H_z is a vertical stretching factor where $H_z \equiv \partial z/\partial \sigma$; f is the Coriolis parameter; p is the atmospheric pressure; ρ and ρ_0 are the total density of the water and the reference density, respectively; g is the gravitational acceleration; v and v_θ are the molecular viscosity and diffusivity; C represents a tracer quantity (such as the temperature, salt, or suspended sediment); and C_{source} is the tracer source/sink term.

We chose the Rutgers University version [33] in the present study. The model was solved on a horizontal Arakawa-C grid. In terms of time, the ROMS adopts a split-explicit time step scheme, that is, a shorter time step is used to simulate the sea surface changes and barotropic momentum, and a longer time step is used to simulate the temperature, salinity, and baroclinic momentum. The ROMS offers several advection schemes, and in this study, the default advection scheme of the fourth-order central vertical advection and third-order upstream horizontal advection schemes was selected. These advection schemes have been extensively employed in previous studies [34–36] to simulate oceanic processes associated with typhoons, yielding reasonable results. In terms of vertical mixing, the air–sea interface exchange and turbulent mixing parameterization schemes can be selected in the model. The ROMS has been widely used in both academic research and operational oceanographic forecasting.

2.2. Wetting and Drying Method

The wetting and drying method for the ROMS was proposed by Warner, et al. [37]. The method makes the ROMS suitable for shallow water and coastal environments. The method is performed at each time step of the barotropic engine, and the sum of the local bathymetry (*h*) and the free-surface displacement (*zeta*) at the grid center is calculated as the total depth of the water (*D*; *D* = *h* + *zeta*). Subsequently, the total depth of the water *D* is compared to the D_{crit} parameter (D_{crit} is the minimum depth defined by the user). If *D* is less than D_{crit}, then the cell is considered 'dry,' and no flux of water is allowed to flow out of that cell for that barotropic time step. The method always allows water to flow into any 'dry' cell at any time, allowing any cell that was previously 'dry' to become 'wet'. Therefore, this method is suitable for intertidal areas where tidal action is significant.

In order to resolve the coastal topography, the ROMS uses the land/sea masking array approach, which sets the value of the land mask to 0 and the value of the sea mask to 1. In the ROMS, the land mask and sea mask are set before the simulation, and the land/sea masking array is spatially invariant during the calculation. For wetting and drying, the method adds an additional wet/dry mask that is independent of the land/sea mask. The spatial variation of the wet/dry mask is carried out on the sea grid (where land/sea mask = 1), with the value of the dry mask set to 0 and the value of the wet mask set to 1.

Since the land/sea mask of the ROMS is spatially invariant, adjustments to the ROMS land/sea mask are required when conducting storm surge inundations. The study uses a maximum inundation elevation (20 m), allowing seawater to submerge land up to a maximum height of 20 m. The ROMS grid's bathymetry is modified based on the maximum inundation elevation, and then a land/sea mask with a specific submerged space is generated. It should be mentioned that before running, the free surface of the initial and the boundary field should be moved to the real level surface.

2.3. Asymmetric Tropical Cyclone (TC) Wind Model

In this study, the Holland wind field model [30] was used to construct ideal typhoons, which were used to provide the atmospheric forcing for the ROMS. In 1954, Schloemer [38] proposed a model of the exponential distribution of hurricane pressure profiles. Based on Schloemer's study, Holland [30] conducted statistical analyses and research on multiple instances of hurricanes in 1980 and found that the pressure difference at the center of these hurricanes varies exponentially along the radius direction. It is worth noting that the change rate in the pressure difference varies for hurricanes of different categories. To address this issue, Holland introduced a parameter, *B*. The pressure gradient's radial profile equation can be written as the following.

$$P(r) = P_c + (P_n - P_c) \times e^{\left(-\frac{R_{\max}}{r}\right)^B} \tag{7}$$

where *P(r)* is the surface pressure at the radius *r*; P_c is the tropical cyclone's central pressure; P_n is the external pressure; *e* is the base of the natural logarithms; $R_{\max}$ is the radius of the maximum winds; *B* is the Holland *B* parameter.

The gradient wind profile equation can be written as the following.

$$V_g(r) = \sqrt{100 \times (P_n - P_c)\frac{B}{\rho}\left(\frac{R_{\max}}{r}^B\right) \times e^{\left(-\frac{R_{\max}}{r}\right)^B} + \left(\frac{rf}{2}\right)^2} - \left(\frac{rf}{2}\right) \tag{8}$$

where $V_g(r)$ is the gradient wind at the radius *r*; ρ is the air density; *f* is the Coriolis parameter, and $f = 2\omega\sin(\varphi)$, where ω is the rotational frequency of the Earth and φ is the latitude.

The maximum wind speed at the gradient level can be written as the following.

$$V_{g\_max} \approx \sqrt{\frac{B \cdot (P_n - P_c)}{e\rho}} \quad (9)$$

The radius to maximum winds and the Holland B parameter can be determined using the calculation method proposed by Vickery and Wadhera [39]. Based on Powell, et al. [40], Vickery and Wadhera [39] combined the pressure data of aircraft detection and HRD (Hurricane Research Division) hurricane wind field observation data to statistically analyze the hurricane characteristic parameters, and proposed the statistical models of the radius to maximum winds and the Holland B parameter. The radius to maximum winds equation can be written as the following.

$$\ln(R_{\max}) = 3.015 - 6.291 \times 10^{-5} \cdot (P_n - P_c)^2 + 0.0337 \cdot \phi \quad (10)$$

where ϕ is the latitude of the tropical cyclone center. Vickery and Wadhera [39] also analyzed the errors of the regression model (10). The difference between the regression model estimates and the data indicates that the model error ($\sigma_{\ln R\max}$) reduces as $\Delta p = P_n - P_c$ increases, as shown in Equation (11). Considering that there may be differences between individual typhoons and the regression model, adjustments to the radius to maximum winds are allowed within a certain range of error.

$$\begin{cases} \sigma_{\ln R_{\max}} = 0.448, \quad \Delta p \leq 87hPa \\ \sigma_{\ln R_{\max}} = 1.137 - 0.00792\Delta p, \quad 87hPa < \Delta p \leq 120hPa \\ \sigma_{\ln R_{\max}} = 0.186, \quad \Delta p > 120hPa \end{cases} \quad (11)$$

The Holland B parameters can be calculated as the following.

$$B = 1.881 - 0.00557 \cdot R_{\max} - 0.01295\phi \quad (12)$$

Using the Holland model to simulate a tropical cyclone, we could obtain an axisymmetric tropical cyclone pressure field and storm vortex at the gradient level. In the classical parametric cyclone model, the cyclone wind field at the gradient level is usually composed of two different wind fields. One is the storm's movement (wind field) at the gradient level caused by the migration of tropical cyclones, and the other is the storm vortex (wind field) at the gradient level obtained by the cyclone's balance [41]. Therefore, the wind field at the gradient level V can be written as the following.

$$V = V_m + V_g \quad (13)$$

where V_g is storm vortex at the gradient level and V_m is the storm's movement at the gradient level.

The exponential function formula established by Miyazaki [42] can be used to calculate the V_m.

$$V_m = V_{TC} \cdot \exp(-\frac{\pi r}{10R_{\max}}) \quad (14)$$

where V_{TC} is the moving velocity vector of the cyclone center and r is the distance from the cyclone center.

The wind field at the gradient level can be obtained using the above calculation, but the ROMS needs to provide the wind field at the surface level (10 m) to calculate the sea surface momentum stress. Based on the logarithmic wind profile model, Pande, et al. [43] used the Boundary Layer Wind Tunnel Laboratory's tropical cyclone model to reconstruct some tropical cyclone cases and developed an alternative approach to model the hurricane boundary layer. The ratio of the wind speed at any height z with the wind speed at the gradient level is represented as the following.

$$V_z = V_g \cdot 0.285(R_0')^{0.07} \ln(\frac{z}{z_0}) \tag{15}$$

$$R_0' = \frac{f \cdot z_0}{V_g} + \left(1 - \frac{V_{TC} \sin \alpha}{V_g}\right) \frac{z_0}{r} \tag{16}$$

where V_z is the surface wind speed at a height z; z_0 is the surface roughness length; R_0' is an equivalent Rossby number; α is the angle between the tropical cyclone track and any point at a radial distance r, measured positive clockwise from the direction of translation.

The calculated wind field needs to be decomposed into meridional wind and zonal wind for the ROMS, thus Equation (13) can be rewritten as the following.

$$V_u = C_1 V_{\mathrm{m}} \cos \varphi - C_2 V_g \sin(\theta + \beta) \tag{17}$$

$$V_v = C_1 V_{\mathrm{m}} \sin \varphi + C_2 V_g \cos(\theta + \beta) \tag{18}$$

where, u and v are the zonal wind component and the meridional wind component, respectively; θ is the angle between the line connecting the grid point, the tropical cyclone center and the east direction (counterclockwise); φ is the angle between the tropical cyclone moving direction and the east direction (counterclockwise); and β is the inflow angle. The National Weather Service's (NWS) representation of the inflow angle [44] can be adopted as follows.

$$\beta = \begin{cases} 10\left(\frac{r}{R_{\max}} + 1\right), & 0 \le r \le R_{\max} \\ 25\left(\frac{r}{R_{\max}}\right) - 5, & R_{\max} \le r \le 1.2R_{\max} \\ 25, & r \ge 1.2R_{\max} \end{cases} \tag{19}$$

C_1 and C_2 are the attenuation factors in Equations (17) and (18), which are the empirical surface wind reduction factors (SWRF) that convert the storm's movement and storm vortex from the gradient level to the surface level, respectively. Two methods are available to convert the wind field from the gradient level to the surface level (10 m). The first method uses the empirical surface wind reduction factors C_1 and C_2 (SWRF C_1 and SWRF C_2) to convert the storm's movement and storm vortex from the gradient level to the surface level, respectively. SWRF C_1 can refer to the values of Wei, et al. [45] and Wang, et al. [44], while SWRF C_2 is summarized in Vickery, et al. [46]. In this method, Equations (15) and (16) are not required. The second method utilizes Equations (15) and (16) to convert the wind field from the gradient level to the surface level (10 m). Therefore, the SWRF C_1 and C_2 unify when this method is used.

In addition, for the reduction in the wind speed at the surface level (10 m) as the storm moves from the sea to the land, Vickery, et al. [46] also summarized the reduction factor of the mean wind speed at 10 m (sea–land transition). We selected the reduction factor of the mean wind speed at 10 m (sea–land transition) proposed by Vickery, which was 20% (at the coast). Therefore, before the typhoon makes landfall, C_1 and C_2 remain the same, and after landfall, they are reduced by 20%: C_1 = 0.8 C_1 and C_2 = 0.8 C_2.

2.4. Model Configuration and Data

2.4.1. Model Configuration

In this study, the hydrodynamic model ROMS was used to study storm surges in the coastal area of Ningbo, China (Figure 1). The main model configuration is shown in Table 1. The simulation area was 28.9° N–30.4° N, 121.2° E–123.0° E. The horizontal resolution was approx. 210 m with 780 × 720 grid cells, and the maximum water depth was 169 m. The model was divided into 15 layers in the vertical direction. The total simulation time was 6 days, and the first 24 h of the simulation were taken as the model spin-up time. The baroclinic time step used in the model was 5 s, and the barotropic time step was 1 s. The mixed radiation-nudging boundary condition was adopted for the free surface, temperature, and salinity [47]. The vertical mixing scheme selected the generic length scale (GLS) vertical mixing scheme [48]. The minimum depth of wet/dry conversion D_{crit} was set to 0.1 m. The bottom friction formula adopted the quadratic bottom friction formula.

$$\tau_{bx} = \left(\gamma_2 \sqrt{u^2 + v^2}\right) u \tag{20}$$

$$\tau_{by} = \left(\gamma_2 \sqrt{u^2 + v^2}\right) v \tag{21}$$

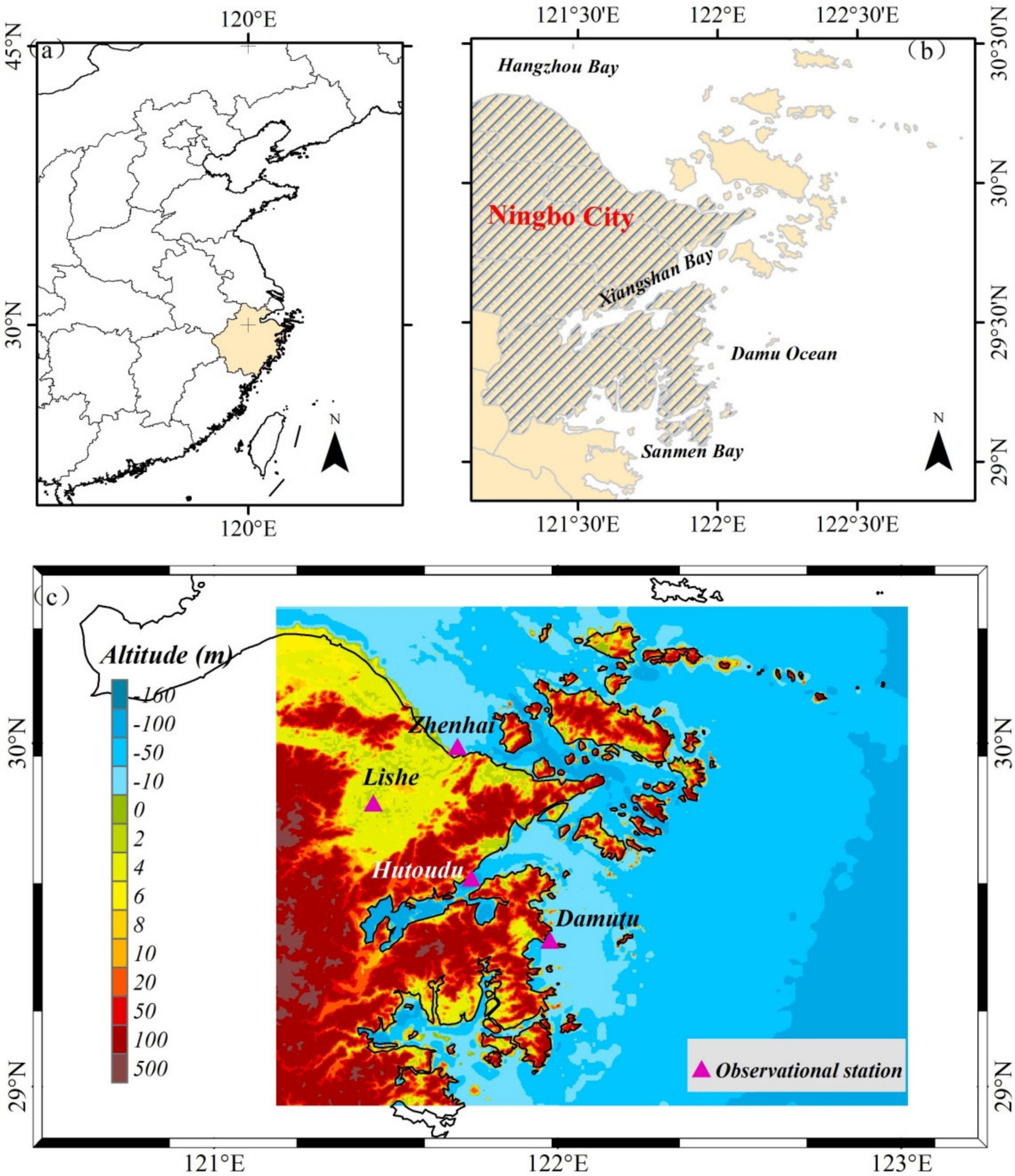

Figure 1. (**a**) Location of Zhejiang Province; (**b**) Location of Ningbo City; (**c**) The study domain with terrain elevation in the present study. The pink triangles show the locations of the weather station (Lishe) and the ocean tidal stations (Zhenhai, Hutoudu, and Damutu).

Table 1. Model configuration.

Item	Configuration
Domain center	122° N, 29.8° E
Resolution	200 m
Grid points	780 × 720
Time step	5 s
Advection scheme	Third-order upstream horizontal advection
	Fourth-order centered vertical advection
Boundary condition	Radiation-nudging (free surface)
Vertical mixing scheme	GLS (k-ε)
Minimum depth for wetting and drying	0.1 m

The quadratic drag coefficient method [49,50] depends only on the velocity components u and v in the bottom grid cell and the constant, spatially uniform coefficient γ_2. The quadratic drag coefficient technique can provide a more stable simulation of ocean bottom friction, making the model more stable and improving the accuracy of the simulation results.

2.4.2. Data Sources

The initial and boundary conditions of the ROMS were provided by the 1/12° HYbrid Coordinate Ocean Model data (HYCOM, https://www.hycom.org/dataserver; accessed on 25 February 2023). The bathymetric topographic data were from the General Bathymetric Chart of the Oceans (https://www.gebco.net/data_and_products/gridded_bathymetry_data/; accessed on 23 February 2023) global bathymetric dataset. The tidal forcing conditions for the ROMS used the TPXO9-atlas data from the Oregon State University Tidal Prediction Software (OTPS) [51], a global tidal reconciliation database (https://www.tpxo.net/global/tpxo9-atlas; accessed on 17 February 2022). The atmospheric forcing of the ROMS model was derived from the reanalysis dataset NCEP FNL (National Centers for Environmental Protection Final Operational Global Analysis) (https://rda.ucar.edu/datasets/ds083.3/; accessed on 7 April 2023) with a 0.25° × 0.25° horizontal resolution. The land use classifications were provided by the MCD12Q1 dataset (https://ladsweb.modaps.eosdis.nasa.gov; accessed on 12 December 2022) retrieved from the MODIS Terra and Aqua satellites. This dataset provided several land cover classification standards, with the IGBP classification standard [52] adopted in this study. The IGBP classification standard contained 17 main land cover types, according to the International Geosphere-Biosphere Programme [52], including 11 natural vegetation types, two developed land types, one mosaic land type, and three non-vegetated land types. We converted these land cover types into the surface roughness length, according to the conversion table [53] from the Weather Research and Forecasting Model (WRF). The typhoon's best track data were from China Meteorological Administration (CMA). The weather station data were from the National Climatic Data Center (ftp://ftp.ncdc.noaa.gov/pub/data/noaa/isd-lite/; accessed on 23 February 2023). The coastal weather station data were from the China National Marine Science Data Center (https://mds.nmdis.org.cn/pages/home.html; accessed on 7 May 2023). The water level data at the tidal stations were from the Ningbo Hydrological Bureau. The surface wind speed was recorded at the Lishe and Zhenhai weather stations, and the water level was recorded at the Zhenhai, Hutoudu and Damutu ocean tidal stations.

2.5. Model Experiments

In this study, the storm surge process of Typhoon In-Fa (2106) was selected for analysis. Typhoon In-Fa (202106) originated in the sea area west-northwest of Guam on 23 July 2021 UTC. On 21 July, the typhoon reached its peak intensity with maximum winds of over 45 m s^{-1} and a minimum pressure of 955 hPa at the typhoon center (24.2° N, 127.8° E). In-Fa first landed in Putuo, Zhoushan City, Zhejiang Province, China at 4:30 UTC on

25 July. Its maximum wind speed was 38 m s^{-1} and the minimum pressure at the center was 965 hPa. In-Fa gradually weakened and made a second landfall in Pinghu, Jiaxing City, Zhejiang Province, China at 1:30 UTC on 26 July, with a reduced maximum wind speed of 30 m s^{-1}.

The following five experiments were designed to investigate the inundation caused by typhoon storm surges of different intensities and tracks (Table 2).

Table 2. Description of the simulation experiment configuration.

Simulation	Atmospheric Forcing	Typhoon Intensity	Typhoon Track
NB-EXP1	NCEP reanalysis data	960 hPa	track1
NB-EXP2	Wind field model	960 hPa	track1
NB-EXP3	Wind field model	920 hPa	track1
NB-EXP4	Wind field model	960 hPa	track2
NB-EXP5	Wind field model	920 hPa	track2

Experiment 1 (NB-EXP1): This experiment used the NCEP reanalysis data as the atmospheric forcing for the ROMS to simulate the storm surge inundation caused by Typhoon In-Fa.

Experiment 2 (NB-EXP2): Based on the intensity and track of Typhoon In-Fa, the typhoon wind field was constructed using the asymmetric tropical cyclone wind model, and the results were compared with NB-EXP1.

Experiment 3 (NB-EXP3): Based on the original track of Typhoon In-Fa ('track1' in Figure 2), the typhoon intensity was increased to 920 hPa based on the distance from the nearest point of the landfall area, and the storm surge inundation was investigated.

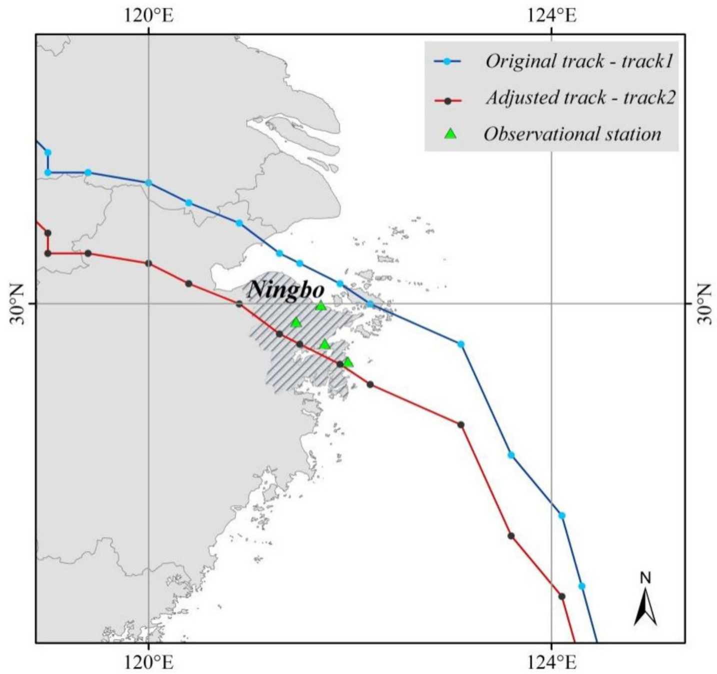

Figure 2. The realistic track of Typhoon In-Fa (blue line) and the adjusted track (red line). Ningbo was located in the south (north) side of the realistic (adjusted) track.

Experiment 4 (NB-EXP4): Based on the original intensity of Typhoon In-Fa, the typhoon track was shifted 0.8 degrees south ('track2' in Figure 2), so that the urban area of Ningbo was exposed to the radius of the maximum winds on the right side (dangerous semicircle) of the typhoon track.

Experiment 5 (NB-EXP5): Based on the Typhoon 'track2', the typhoon intensity was increased to 920 hPa based on the distance from the nearest point of the landfall area.

In the NB-EXP1 experiment, to satisfy the model simulations, we interpolated the NCEP reanalysis data with a 0.25° × 0.25° horizontal resolution into the atmospheric forcing files with the same resolution as the ROMS grids. In the NB-EXP2 through NB-EXP5 experiments, we constructed typhoon wind fields with a 0.05° × 0.05° horizontal resolution using the asymmetric tropical cyclone wind model and then interpolated the wind field into the atmospheric forcing files with the same resolution as the ROMS grids.

We conducted an additional experiment that only considered the tidal effects, which provided a sea surface condition with no wind and normal air pressure. By subtracting the simulation results of only the tides from the free sea surface of NB-EXP2 through NB-EXP5, we obtained the results of only the storm surge.

2.6. Statistics for the Model–Measurement Comparison

This study introduced three statistical measures to assess the model performance versus the observations: the mean bias (*MB*), root mean square error (*RMSE*), and index of agreement (*IOA*). The equations for these three parameters are written as the following.

$$MB = \frac{1}{N}\sum_{i=1}^{N}(P_i - O_i) \tag{22}$$

$$RMSE = \left[\frac{1}{N}\sum_{i=1}^{N}(P_i - O_i)^2\right]^{\frac{1}{2}} \tag{23}$$

$$IOA = 1 - \frac{\sum_{i=1}^{N}(P_i - O_i)^2}{\sum_{i=1}^{N}\left(\left|P_i - \overline{O}\right| + \left|O_i - \overline{O}\right|\right)^2} \tag{24}$$

where P_i is the simulated variables, O_i is the observed variables, N is the total number of the predictions used for the comparisons, and $\overline{O}$ represents the average of the observations. The *IOA* varies from 0 to 1, and a higher *IOA* indicates a better agreement between the simulation and the observation.

3. Results and Discussion

3.1. Wind Field Simulations

The typhoon wind fields at the surface level of the five experiments were provided by the NCEP reanalysis data and the asymmetric TC wind field model, respectively (Figure 3). Figure 3a (NB-EXP1) and Figure 3b (NB-EXP2) show that the typhoon wind field constructed using the asymmetric TC wind field model had a more refined typhoon structure near the typhoon center than that of the NCEP reanalysis data, which was attributed to the low spatial resolution of the NCEP reanalysis data (0.25° × 0.25° horizontal resolution). The spatial distribution in the NB-EXP1 experiment indicated that the wind speed on the left and right sides of the typhoon motion track were different, and the wind speed on the right half (dangerous semicircle) was significantly higher than that on the left half (navigable semicircle). In the NB-EXP2 experiment, the spatial wind speed distribution of the wind field (wind field = circular symmetrical storm vortex + storm's movement) was similar to that in the NB-EXP1 experiment. Figure 3b shows that there was a difference in the wind speed between the land and sea surfaces, which was mainly due to the use of the Equation (15). Due to the different types of land use cover, the land surface roughness was higher than the sea surface roughness, so the land absorbed more wind energy, resulting in a decrease in the wind speed. This phenomenon was also consistent with the distribution characteristics of the wind speed over the land and sea in the NB-EXP1 experiment. The maximum surface the wind speed of Typhoon In-Fa in the NB-EXP1 experiment (26.79 m s^{-1}) was less than that in the NB-EXP2 experiment (31.60 m s^{-1}) at the time of landfall (04:00 UTC on 25 July). When the typhoon intensity rose to 920 hPa (NB-EXP3), the maximum wind speed reached 48.39 m s^{-1} in the NB-EXP3 experiment. We compared the spatial wind speed distribution in the NB-EXP2 (Figure 3b) and NB-EXP3 (Figure 3c) experiments, and we showed that the dangerous semicircle range in the NB-EXP3 experiment was obviously smaller than that in the NB-EXP2 experiment. However, the wind speed was greater than that in the NB-EXP2 experiment. As expressed in Equation (10), when the typhoon intensity increased, the radius of the maximum winds decreased. The adjusted typhoon track (track2) is adopted in the NB-EXP4 and NB-EXP5 experiments. Figure 3d,e show that the offset of the typhoon track almost completely exposes the urban area of Ningbo to the dangerous semicircle. At 04:00 UTC on 25 July, the maximum wind speeds in the NB-EXP4 and NB-EXP5 experiments were 32.10 m s^{-1} and 48.96 m s^{-1}, respectively.

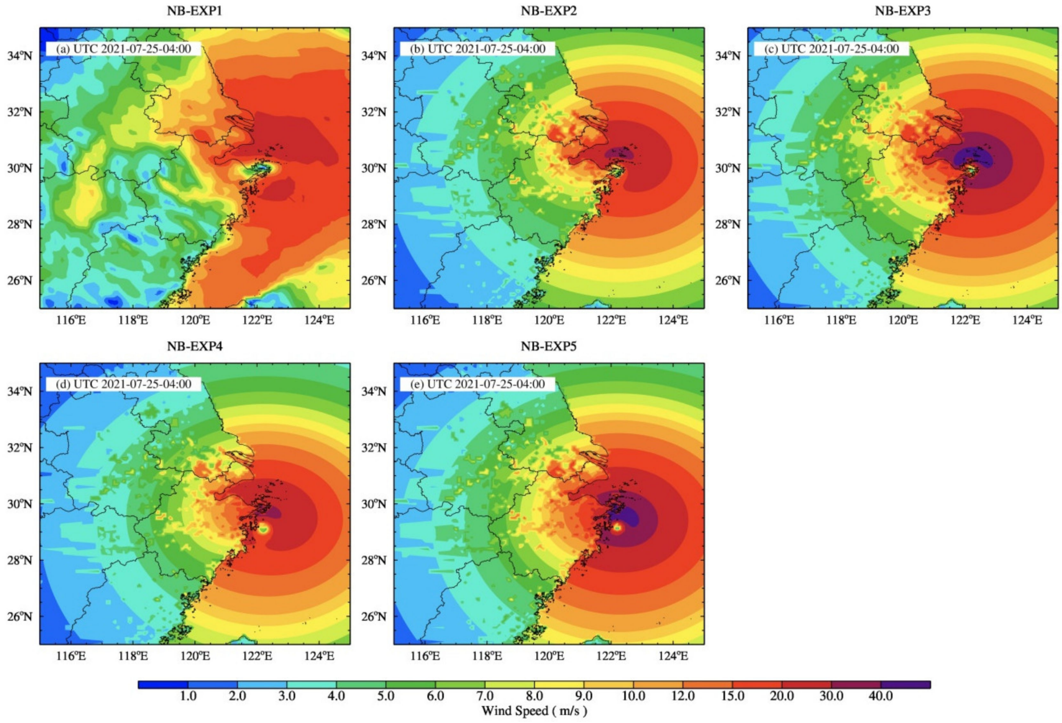

Figure 3. The spatial distributions of the 10 m wind speed at 04:00 UTC on 25 July 2021 (landing) in the five experiments.

We compared the wind speed simulated in the NB-EXP1 and NB-EXP2 experiments to the observations at the Lishe and Zhenhai weather stations (Figure 4). The RMSE and IOA for these two stations indicated that the wind speed simulated in the NB-EXP1 and NB-EXP2 experiments matched the observations well. The wind speed at the Lishe station in the NB-EXP1 experiment was slightly overestimated relative to the observed wind speed (MB = 0.88 m s^{-1}), and the predicted maximum wind speed appeared earlier than the observations. This was mainly attributed to the low spatial resolution of the NCEP reanalysis data, which could not demonstrate the local wind field observed at the weather station very well. At the Zhenhai station, the maximum wind speed simulated in the NB-EXP1 experiment was slightly underestimated compared to the maximum wind speed observations. The timing of the wind speed decline appeared earlier than the observations, mainly due to the low spatial resolution. As shown in Figure 4c, the observations at the Zhenhai station indicated a trough in the wind speed observation at 16:00 UTC on 25 July. Both the NB-EXP1 and NB-EXP2 experiments captured this phenomenon. On the other hand, it can be seen from both Figure 4a,c that although the moment of the maximum wind speed simulated in the NB-EXP2 experiment aligned with the moment of the observed maximum wind speed, it should be noted that the wind speed in the NB-EXP2 experiment at the initial time was underestimated relative to the observations. The reason was the fast decay of a constructed wind field from the typhoon center to the periphery using the Holland model [54–56].

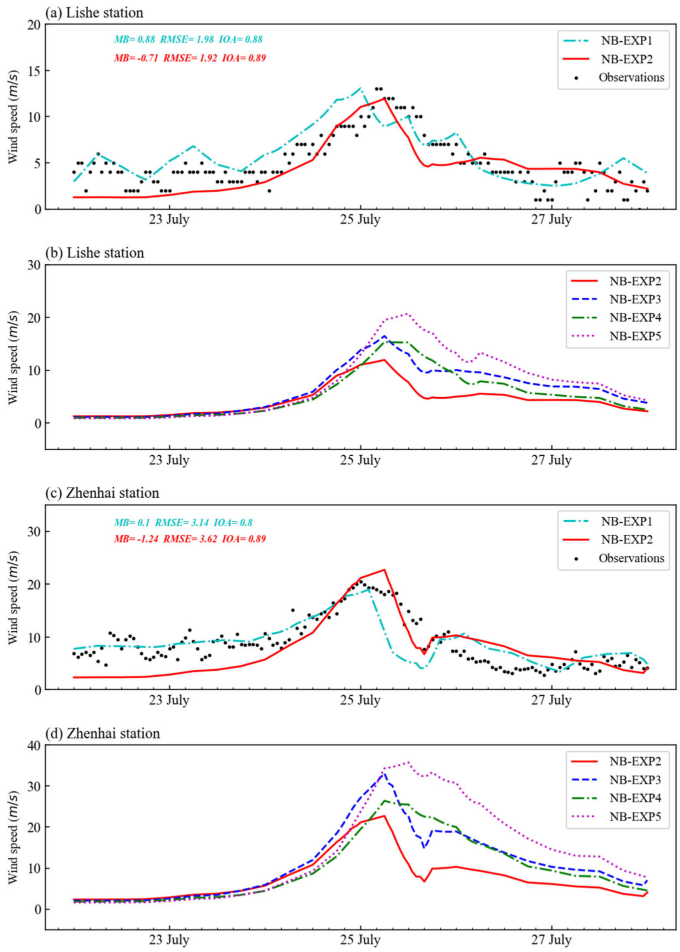

Figure 4. (**a**) Simulated wind speeds in the NB-EXP1 and NB-EXP2 experiments vs. observations at the Lishe weather station; (**b**) a comparison of the simulated wind speeds at the Lishe weather station among the different model experiments; (**c**) simulated wind speeds in the NB-EXP1 and NB-EXP2 experiments vs. observations at the Zhenhai weather station; (**d**) a comparison of the simulated wind speeds at the Zhenhai station among the different model experiments.

The NB-EXP2 through NB-EXP5 experiments used the wind field model to provide the forcing and consider the impact of the surface roughness on the winds. In the NB-EXP2 experiment, the maximum wind speed at the Lishe station was lower than that at the Zhenhai station (Figure 4a,c), which was consistent with the observations. Since the Lishe station was located at an airport and the Zhenhai station was located near the sea, the local land covers were different. 'Urban and Built-Up' had a higher surface roughness length than 'Water'. Therefore, Equations (15) and (16) considered the impact of the land cover on the wind speed, while the empirical reduction factors did not, so the wind speed on the land calculated by the empirical reduction factors could have been overestimated.

Figure 4b,d illustrate the variations of the simulated wind speed at the Lishe station and the Zhenhai station across the various typhoon tracks and intensities (NB-EXP2, NB-EXP3, NB-EXP4 and NB-EXP5), respectively. We compared the wind speed at the Lishe station (Figure 4b) in the NB-EXP3 and NB-EXP4 experiments, and it was shown that despite the increase in the typhoon intensity to 920 hPa in the NB-EXP3 experiment, the predicted wind speed was still not significantly higher than that of the weaker typhoon in the NB-EXP4 experiment (960 hPa). This indicated that the severity of the impacted region during the typhoon was closely linked to its position concerning the typhoon. When the impacted region was located in the dangerous semicircle of the typhoon, it suffered greater wind damage. The wind speed of a Category 2 typhoon within a dangerous semicircle could approach or exceed that of a Category 3 or 4 typhoon within the navigable semicircle. In addition, Figure 4b,d both show that the strong wind duration in the NB-EXP4 experiment was longer than that in the NB-EXP2 experiment, and the same was true for the comparison between the NB-EXP5 experiment (920 hPa) and the NB-EXP3 experiment (920 hPa). This indicated that the impacted region, which was located in the dangerous semicircle during the typhoon's life, suffered from longer durations of strong wind attacks.

3.2. Storm Surges and Water Level Variations

We compared the predicted water levels in the NB-EXP1 and NB-EXP2 experiments during the period from 23 July to 28 July 2021 with the observations at the three ocean tidal stations (Zhenhai, Hutoudu, and Damutu in Ningbo) in the simulation domain (Figure 1). Figure 5 shows that the NB-EXP1 and NB-EXP2 experiments yielded the observed water level fluctuations, with a high IOA of 0.96–0.98. The difference between the simulated maximum water level at each station in NB-EXP2 and the observations was approx. 0.3 m. Moreover, the water level at the three ocean tidal stations in the tidal trough rose significantly during the typhoon's passage (around 25 July), but the overall tidal cycle remained unchanged, indicating that the typhoon mainly affected the height of the water level and had little effect on the original astronomical tide cycle [57].

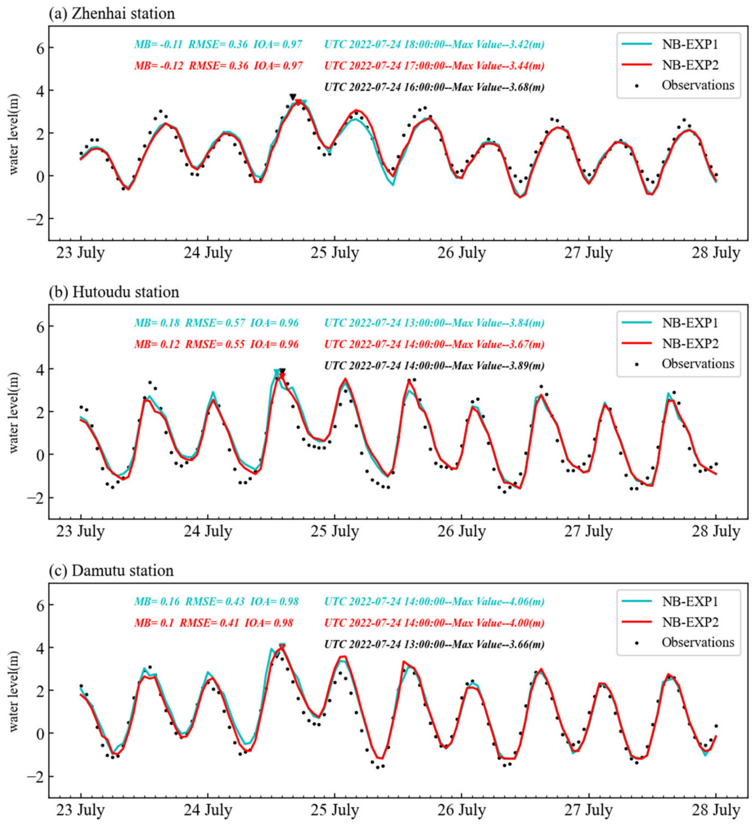

Figure 5. Temporal variations of the simulated (curves) and measured (black dots) water levels at the three ocean tidal stations, including Zhenhai, Hutoudu, and Damutu.

3.2.1. Positive and Negative Storm Surges

Figure 6 displays that the simulated storm surge at the three stations in the NB-EXP2 experiment was not significant. The most notable positive storm surge occurred at the Zhenhai station, reaching a maximum value of 1.35 m. As a comparison, negative storm surges appeared at the other two stations. An increase in the typhoon intensity to 920 hPa along the original track (tarck1) resulted in a higher maximum storm surge of 2.22 m at the Zhenhai station in the NB-EXP3 experiment. Interestingly, the storm surge at the Zhenhai station in the NB-EXP3 exhibited an increase and a subsequent decrease (Figure 6a), while Hutoudu and Damutu experienced severe negative storm surges, with a maximum negative storm surge of over 1.5 m at the Damutu station (Figure 6c). This phenomenon can be attributed to the fact that the three stations were located on the left side of the typhoon track in the NB-EXP3 experiment. Before the typhoon passed, the Zhenhai station was mainly affected by onshore winds, resulting in significant positive storm surges. After the typhoon passed, the station was affected by offshore winds, leading to negative storm surges. On the other hand, the Hutoudu and Damutu stations were influenced by the northwest offshore winds for a considerable time, resulting in no significant positive storm surges, but long-duration negative storm surges instead.

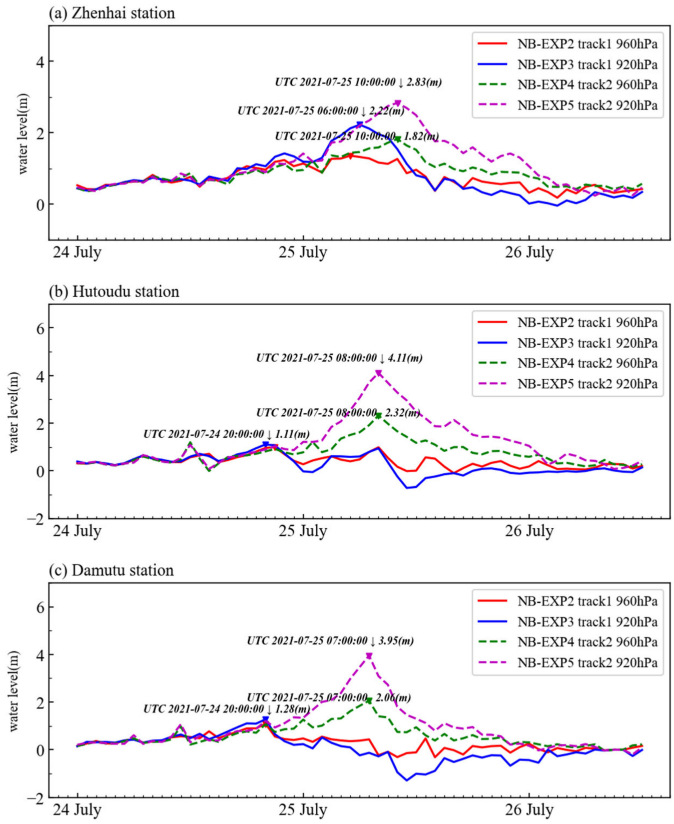

Figure 6. Temporal variations of the storm surges in NB-EXP2 (red solid line), NB-EXP3 (blue solid line), NB-EXP4 (green dashed line), and NB-EXP5 (pink dashed line).

In the NB-EXP4 experiment, we maintained the intensity of Typhoon In-Fa but moved the typhoon track to track2, placing all three stations in the dangerous semicircle. Figure 6b,c show that the storm surges transitioned from the negative phase to the positive phase at both the Hutoudu and Damutu stations. The reason for this phenomenon was that, due to the typhoon track's offset, the area where the two stations were located was subjected to extremely high wind speeds in the dangerous semicircle and was also influenced by the southeast onshore winds on the right side of the typhoon for a long time, resulting in significant positive storm surges. The simulated maximum positive storm surges in the NB-EXP4 experiment were 2.32 m and 2.06 m at the Hutoudu and Damutu stations, respectively, while the storm surge at the Zhenhai station in the NB-EXP4 experiment was 1.82 m, which was less than the NB-EXP3 experiment. The NB-EXP5 experiment enhanced the intensity of the typhoon on the basis of NB-EXP4, so that the predicted maximum positive storm surges at Zhenhai, Hutoudu and Damutu stations were 2.83 m, 4.11 m and 3.95 m, respectively, which were remarkably stronger than those in NB-EXP4.

3.2.2. Water Level Variations

Figure 7 demonstrates the temporal variations of the total water levels caused by the storm surge superimposed tides and the different typhoon intensities and tracks in NB-EXP2, NB-EXP3, NB-EXP4, and NB-EXP5. We compared the water level changes caused by the different tracks (track1 and track2) with the same intensity (960 hPa) and observed that the water level in the NB-EXP4 experiment was generally higher than the NB-EXP2 experiment around the typhoon landfall time (4:30 UTC on 25 July). This trend was particularly clear in the maximum water levels at the Hutoudu and Damutu stations. The maximum water levels at the Hutoudu and Damutu stations in the NB-EXP4 were 4.02 m and 4.27 m, respectively, which were higher than the maximum water levels in the NB-EXP2, which were 3.67 m and 4.00 m.

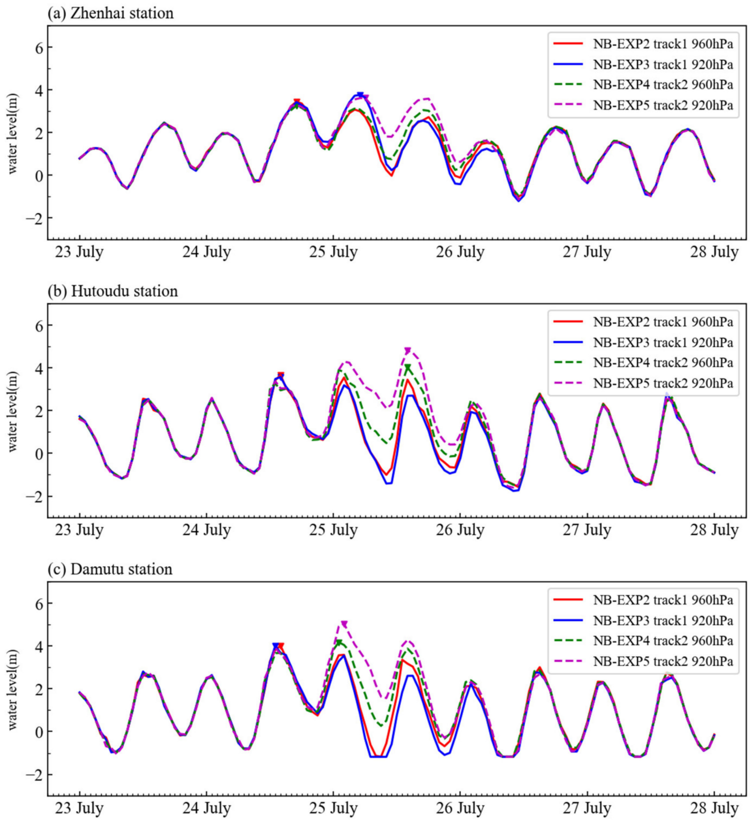

Figure 7. Temporal variations of the simulated water levels in NB-EXP2 (red solid line), NB-EXP3 (blue solid line), NB-EXP4 (green dashed line), and NB-EXP5 (pink dashed line).

Notably, our experimental results demonstrated that a stronger typhoon (920 hPa) caused a more severe minimum water level under track1 (NB-EXP3). For example, the minimum water level reached −1.76 m at the Hutoudu station in the NB-EXP3 experiment. The wet/dry method in the ROMS identified this grid as a 'dry' grid when the water level at the Damutu station was as low as −1.20 m in the NB-EXP3 experiment. In addition, the maximum water levels at the Hutoudu and Damutu stations in the NB-EXP5 experiment reached 4.81 m and 5.04 m, respectively. However, the maximum water level at the Zhenhai station in the NB-EXP5 experiment was 3.62 m, which was less than the 3.76 m maximum water level at the Zhenhai in the NB-EXP3 experiment. The main reason for this was that the maximum water level time at the Zhenhai in the NB-EXP5 experiment was close to or coincided with the trough time of the tide.

3.3. Storm Surge Inundation

Figure 8 illustrates the spatial distribution of the water levels during the maximum water level time at the Hutoudu station in NB-EXP2 through NB-EXP5. By comparing

Figure 8c,g, it was evident that adjustments in the typhoon track resulted in changes in the value and timing of the maximum water level observed at the Hutoudu station. According to the information presented in Figure 8a, the water level in the Xiangshan Bay exceeded 3.5 m at 14:00 UTC on 24 July. As shown in Figure 8b, the distribution of the high water level (exceeding 3.5 m) in the NB-EXP3 experiment was slightly wider than that in the NB-EXP2 experiment. At 14:00 UTC on 24 July, the inundation area in the study area was 30.29 km^2 for the NB-EXP2 and 33.34 km^2 for the NB-EXP3 experiments, respectively. Adjusting the typhoon track to track2 revealed that in NB-EXP4 (Figure 8e), an obvious high water level was recorded on the right side of the typhoon track. At 14:00 UTC on 25 July, the maximum water level exceeded 4 m in the Xiangshan Bay, while the water level on the left side along the typhoon track was relatively low (near the Sanmen Bay). This phenomenon was more evident under the stronger typhoon in the NB-EXP5 (Figure 8f), where the maximum water level in most of the long and narrow bay where the Xiangshan Bay was located exceeded 4 m. The water level at the Hutoudu station reached its peak at 14:00 UTC on 25 July in the NB-EXP4 and NB-EXP5 experiments, where the inundation area in the whole study area was 44.97 km^2 and 109.59 km^2, respectively.

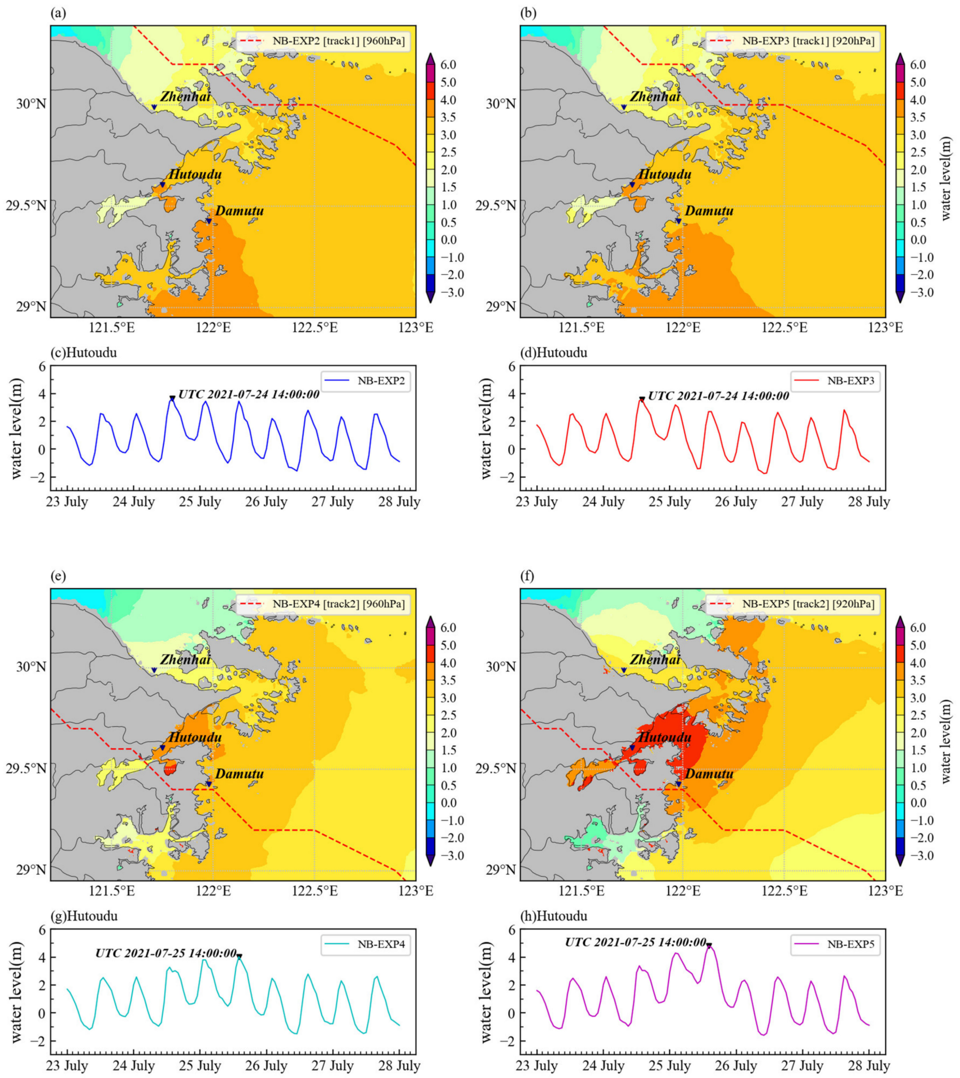

Figure 8. Spatial distributions of the water levels in NB-EXP2 (**a**), NB-EXP3 (**b**), NB-EXP4 (**e**), and NB-EXP5 (**f**) at the moment when the water level at the Hutoudu station reached the maximum. Temporal variations of the simulated water levels at the Hutoudu station in NB-EXP2 (**c**), NB-EXP3 (**d**), NB-EXP4 (**g**), and NB-EXP5 (**h**).

Figure 9 indicates the spatial distribution of the water levels in the NB-EXP5 experiment at four different moments. As shown in Figure 9a, at the initial time of 00:00 UTC on 23 July 2021, there was no significant impact on the sea surface water level from the NB-EXP5 typhoon. At 02:00 UTC on 25 July, the water level at the Damutu station reached its highest value (Figure 9b). Furthermore, the water levels in the Xiangshan Bay, the Damu Ocean, and the Sanmen Bay exceeded 4 m (Figure 9b). At this moment, the inundation area in the study area was 106.37 km^2 for the NB-EXP5 experiment. The water level at the Zhenhai station reached its peak at 17:00 UTC on 25 July (Figure 9g), and the inundation area in the study area was 97.77 km^2 for the NB-EXP5 experiment.

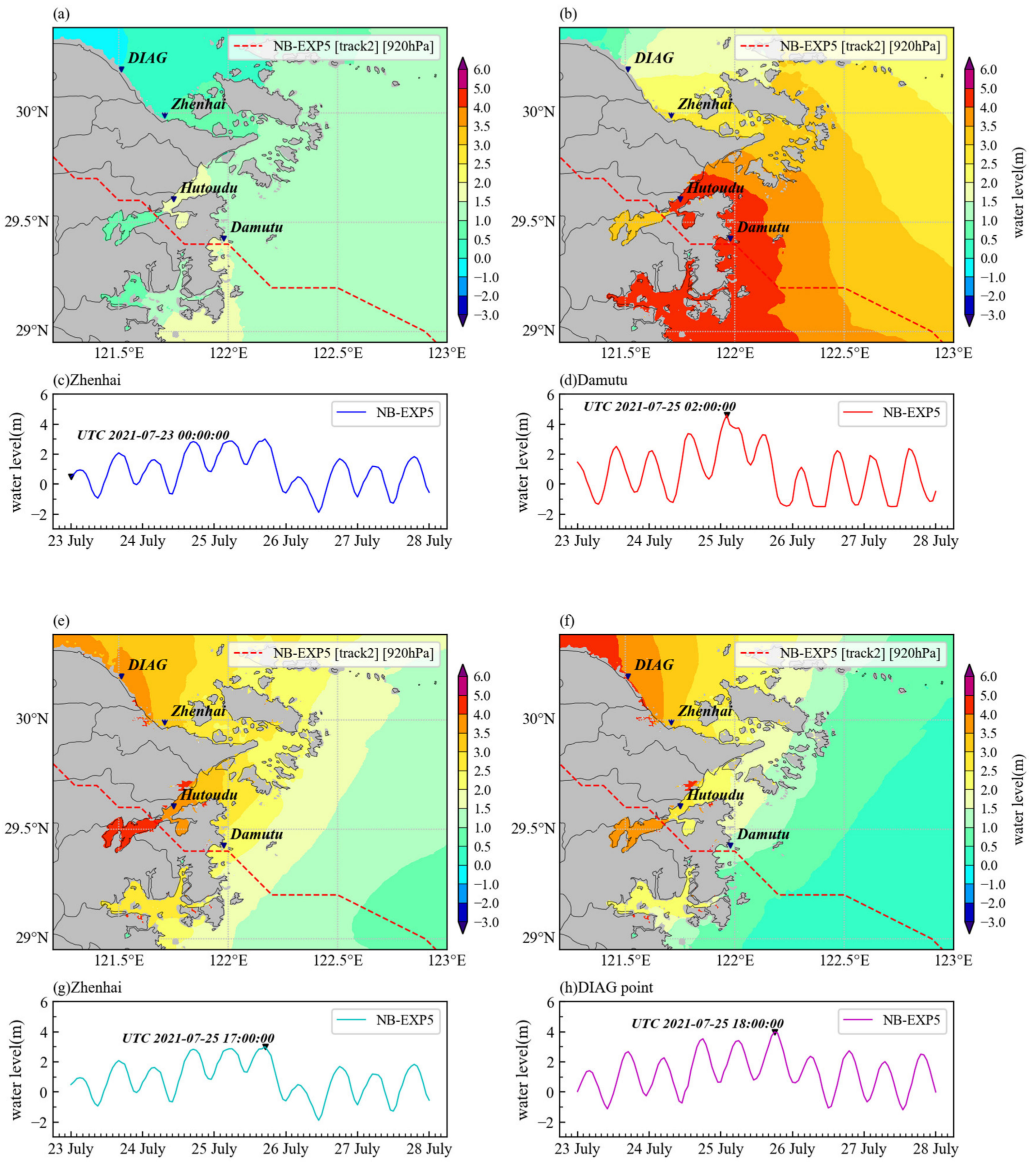

Figure 9. Spatial distribution of the water levels in the NB-EXP5 experiment at four different moments: (**a**,**c**) the initial moment; (**b**,**d**) the moment when the water level at the Damutu station reached the maximum; (**e**,**g**) the moment when the water level at the Zhenhai station reached the maximum; (**f**,**h**) the moment when the water level at the diagnostic point reached the maximum.

We added a diagnostic point called 'DIAG' (as shown in Figure 9f) in the study area to observe the water level changes along the coast of the Hangzhou Bay. At 18:00 UTC on 25 July, the water level at this point reached the maximum water level at 4.31 m. At this moment, the inundation area in the study area was 93.49 km^2 for the NB-EXP5 experiment. Figure 9f also reveals that the maximum water level would gradually increase from the Hangzhou Bay towards the inner part of the Hangzhou Bay. This was due to the convergence effect of the tides in the Hangzhou Bay, resulting in a larger tidal amplitude within the inner bay. If a powerful typhoon caused a storm surge in the Hangzhou Bay, coupled with the huge tidal amplitude, it would result in more severe disasters along the coast of the Hangzhou Bay.

We compared the temporal variations of the inundation area in the whole study area in the NB-EXP2, NB-EXP3, NB-EXP4, and NB-EXP5 experiments. Figure 10 shows that the temporal variations of the inundation area in the NB-EXP2 and NB-EXP3 experiments exhibited two peaks, while the temporal variations of the inundation area in the NB-EXP4 and NB-EXP5 experiments displayed three peaks. The reason for this was mainly due to the different tracks of typhoons. In the NB-EXP3 experiment, the inundation area reached its first peak of 52.52 km^2 at 16:00 UTC on 24 July when the low altitude areas along the coast of the Sanmen Bay and the Damu Ocean were inundated, and its second peak of 46.57 km^2 at 06:00 UTC on 25 July when the low altitude areas near the Zhenhai station were inundated. In the NB-EXP5 experiment, the inundation area reached its first peak of 38.85 km^2 at 15:00 UTC on 24 July when the low altitude areas along the coast of the Sanmen Bay and the Damu Ocean were inundated. The inundation area reached its second peak of 118.187 km^2 at 03:00 UTC on 25 July when the low altitude areas along the coast of the Xiangshan Bay were inundated. The third peak of 119.51 km^2 occurred at 15:00 UTC on 25 July when low altitude areas along the coast of the Zhenhai station were inundated.

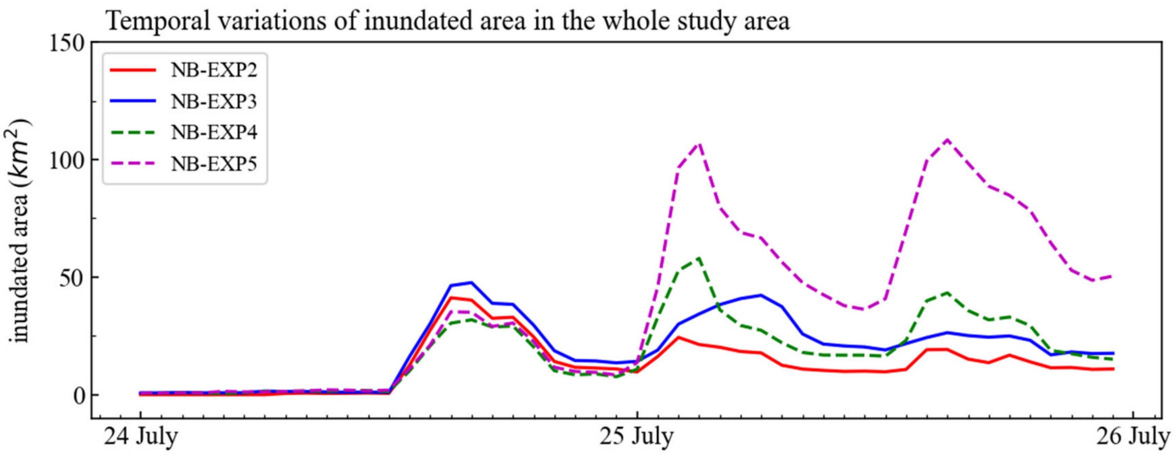

Figure 10. Temporal variations of the inundation area in the whole study area in NB-EXP2 (red solid line), NB-EXP3 (blue solid line), NB-EXP4 (green dashed line), and NB-EXP5 (pink dashed line).

As shown in Figure 11, we further presented the total inundation areas in the study area in the NB-EXP2, NB-EXP3, NB-EXP4, and NB-EXP5 experiments. We retained the maximum water depth at each grid cell (water level envelope) during the typhoon to estimate the total inundation area. The total inundation areas in the NB-EXP2, NB-EXP3, NB-EXP4, and NB-EXP5 experiments were 108.57 km^2, 139.97 km^2, 141.81 km^2, and 245.41 km^2, respectively. Figure 11 also shows the maximum water depth in the inundated region during the typhoon. Compared to the NB-EXP3 experiment (Figure 11b), the NB-EXP5 experiment (Figure 11d) had a wider inundated region and a higher maximum water depth. These results suggested that there was a positive correlation between the strength of a typhoon and the storm surge inundation area. Additionally, the location of the impacted region within the typhoon's wind field played a crucial role in determining the severity of the storm surge. In particular, if an area fell within the dangerous semicircle of the typhoon, it was more likely to experience a severe storm surge disaster.

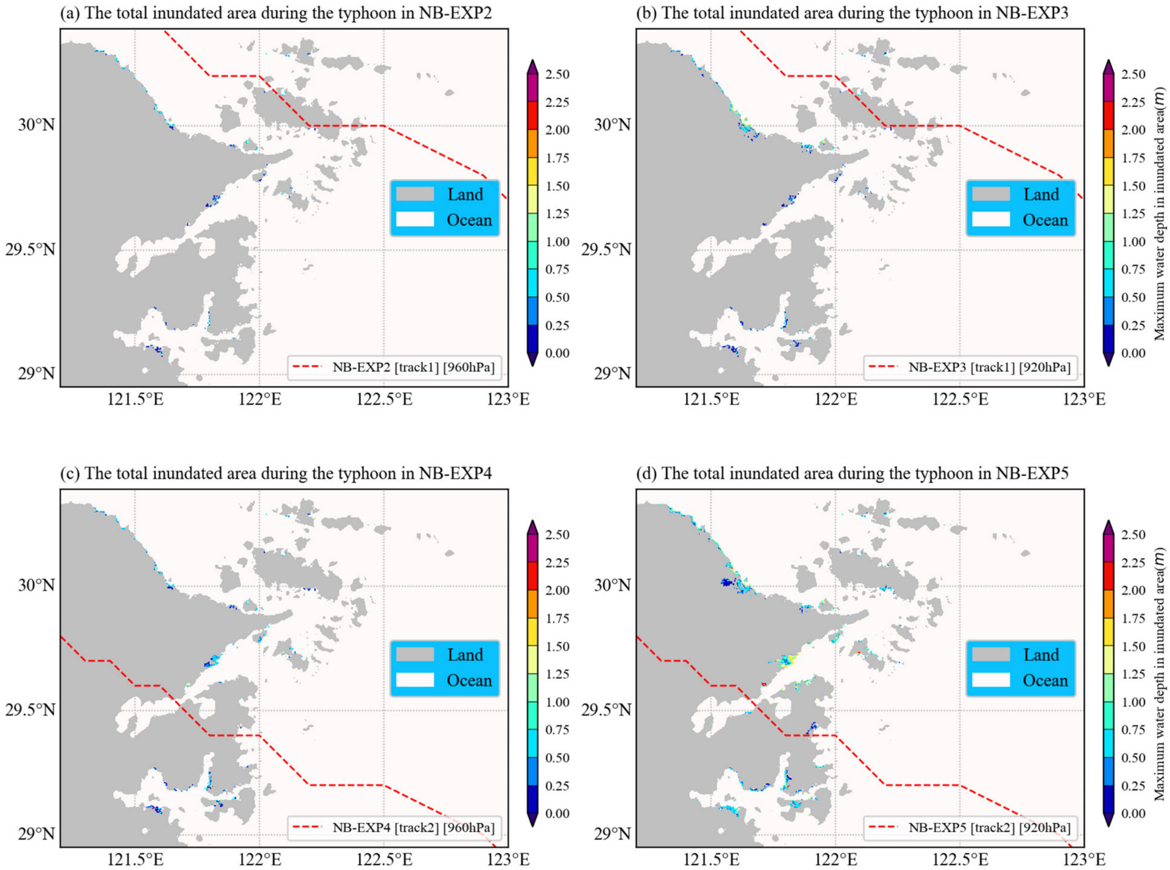

Figure 11. Spatial distributions of the total inundation area during the typhoons in NB-EXP2, NB-EXP3, NB-EXP4, and NB-EXP5.

The size and forward speed of the typhoon are also important factors affecting storm surges [58,59]. As shown in Equations (9) and (12), for the typhoons with the same intensity, a larger typhoon would result in a smaller maximum gradient wind speed. However, larger storm wind fields would cover a wider area of sea, which could also lead to more storm surges [58]. On the other hand, Equations (13) and (14) indicated that when the forward speed of the typhoon increased, the wind speed of the moving wind field superimposed on the gradient wind field would be higher. However, slower storms produced storm surges with a longer duration and wider ranges in the coast (including bays and estuaries). For the three-dimensional circulation model ROMS, a large number of grids and small time steps used in this study made the computation of each experiment very costly. Therefore, further investigations are still needed to determine how the storm's size and forward speed affect storm surges once additional observed data and stronger computational power are available.

In this study, we focused on the effects of land cover on the wind speed but did not account for the land cover variation in the calculation of the bottom friction, which was a limitation of the present work. Zhang, et al. [49] showed that in heavily vegetated and highly developed areas (such as mangrove zones along the coast), surge inundation was reduced due to the increased bottom friction, and the inundation area also decreased significantly. Therefore, the change in bottom friction caused by land cover should also be considered in future studies.

Moreover, waves are also an important factor that affects storm surges. The inclusion of the wave setup in the SLOSH model for storm surges would result in 10–50% higher water levels [60]. The ROMS is a three-dimensional ocean model used primarily to simulate physical processes in the ocean, such as ocean currents, temperature, and salinity. To simulate waves, a wave module such as SWAN (Simulating WAves Nearshore) needs to be coupled with the ROMS [29]. Wu, et al. [24] used a coupled ocean (ROMS)–atmosphere (WRF) wave (SWAN)–sediment transport (COAWST) modeling system to study Typhoon Kai-Tak. They considered that under the extreme conditions of a storm surge caused by a typhoon, the effect of the wave-induced radiation stress on the extreme value of the storm surge was obvious. The amplitude of the wave impact on the storm surge was close to 10%, and the maximum radiation stress occurred at the time of the extreme storm surge. During the storms, both waves and storm surges contribute to coastal inundation. The relative contribution of waves and storm surges depends largely on the coastal environment. For coastal environments with steep slopes, the contribution of waves may be larger than or equal to storm surge inundation [61–63]. However, in places where the continental shelf is wide and shallow with a mild slope, the storm surge may dominate the inundation process, as demonstrated by Rey, et al. [64]. Therefore, to accurately predict and assess the risk of storm surge inundation, the effects of both waves and storm surges need to be considered.

Undoubtedly, factors such as the storm size, forward speed, and waves also play important roles in storm surges. Therefore, these factors should be considered in future studies.

4. Conclusions

In this study, we developed a framework to simulate typhoon storm surge inundation using the Regional Ocean Modeling System (ROMS) for the first time. We established an asymmetric typhoon wind field for the ROMS based on the Holland model, which generated pressure and wind fields during a typhoon. The reanalysis wind data and model wind field were used to drive the storm surge inundation model. Our results showed that the constructed storm surge inundation model could accurately simulate changes in the water level due to storm surges in Ningbo, China during Typhoon In-Fa.

We employed the asymmetric typhoon wind model to construct different typhoon events based on Typhoon In-Fa, aiming to analyze the water level changes and storm surge inundation process regarding the typhoon intensities and tracks. Our results demonstrated that both the intensities and tracks of the typhoon significantly impacted the magnitude of storm surges. When the typhoon intensities were the same, the maximum storm surge region was predominantly determined by the typhoon wind field and the characteristics of the coastline. Specifically, if an area fell on the right side of the typhoon track, it would experience a long duration and high amplitude positive storm surge. However, if an area was located on the left side of the typhoon track, it would experience a short duration and lower amplitude positive storm surge, followed by a negative storm surge. We constructed a wind field that affected the study area based on the intensity and track of Typhoon In-Fa, resulting in a total inundation area of 108.57 km^2. An increase in the typhoon intensity (920 hPa) led to a total inundation area of 139.97 km^2. Comparatively, maintaining the intensity of Typhoon In-Fa while exposing Ningbo to the dangerous semicircle of the typhoon resulted in a total inundation area of 141.81 km^2. Most notably, when Ningbo was exposed to the dangerous semicircle of a stronger typhoon with a central pressure of 920 hPa, the total inundation area would alarmingly reach 245.41 km^2, which would pose a serious threat to life and property along the coast.

Author Contributions: All authors contributed to the manuscript and discussed the results. Conceptualization, G.Q. and T.F.; methodology, G.Q. and T.F.; validation, G.Q. and T.F.; investigation, G.Q., Z.F., S.Z., Y.M. and T.F.; data curation, G.Q., Z.F., S.Z. and Y.M.; writing-original draft, G.Q.; writing-review and editing, Z.F., S.Z., Y.M., W.S., G.Y., L.W. and T.F.; visualization, G.Q.; supervision T.F.; funding acquisition, W.S. and T.F.; All authors have read and agreed to the published version of the manuscript.

Funding: This work was supported by the Natural Science Foundation of Zhejiang Province (no. LZ20D050001), the Natural Science Foundation of Ningbo (no. 2021J083), and the Science and Technology Innovation 2025 Major Project of Ningbo City (no. 20212ZDYF020049 and no. 2022Z189). This study was also sponsored by the K. C. Wong Magna Fund from Ningbo University.

Institutional Review Board Statement: Not applicable.

Informed Consent Statement: Not applicable.

Data Availability Statement: The data presented in this study are available on request from the corresponding author.

Acknowledgments: We are grateful for the provision of the necessary data from the HYbrid Coordinate Ocean Model, the General Bathymetric Chart of the Oceans, NCEP FNL, the global tidal model TPXO, and the MODIS remote sensing products. We are also grateful for the provision of the observed data by the China Meteorological Administration, China National Marine Science Data Center, and the Ningbo Hydrological Bureau.

Conflicts of Interest: The authors declare no conflict of interest.

References

1. El-Sabh, M.I. *Earthquake and Atmospheric Hazards: Preparedness Studies*; Springer Science & Business Media: Dordrecht, The Netherlands, 1998; Volume 16.
2. Li, Y.; Chen, X.; Jiang, X.; Li, J.; Tian, L. Numerical simulations and comparative analysis for two types of storm surges in the Bohai Sea using a coupled atmosphere-ocean model. *Acta Oceanol. Sin.* **2019**, *38*, 35–47. [CrossRef]
3. Chu, D.; Niu, H.; Qiao, W.; Jiao, X.; Zhang, X.; Zhang, J. Modeling Study on the Asymmetry of Positive and Negative Storm Surges along the Southeastern Coast of China. *J. Mar. Sci. Eng.* **2021**, *9*, 458. [CrossRef]
4. Landon, M.E.; Hudyma, N.W.; Sharma, R.S. Hurricane Irma: Consequences of Intense Rainfall and Storm Surge from a Tropical Storm in North and Central Florida. *ISSMGE Int. J. Geoengin. Case Hist.* **2020**, *5*, 26–46. [CrossRef]
5. Li, T.; Wu, S.; Hou, J.; Yu, F. Numerical simulation and risk calculation on storm surge of Ningbo. *Haiyang Xuebao* **2013**, *35*, 9–14. [CrossRef]
6. NBNRP. Ningbo Marine Disaster Bulletin. Available online: http://zgj.ningbo.gov.cn/ (accessed on 25 February 2023).
7. Conner, W.; Kraft, R.; Harris, D.L. Empirical methods for forecasting the maximum storm tide due to hurricanes and other tropical storms. *Mon. Weather Rev.* **1957**, *85*, 113–116. [CrossRef]
8. Hansen, W. Theorie zur Errechnung des Wasserstandes und der Strömungen in Randmeeren nebst Anwendungen 1. *Tellus* **1956**, *8*, 287–300. [CrossRef]
9. Jelesnianski, C.P. "Bottom stress time-history" in linearized equations of motion for storm surges. *Mon. Weather Rev.* **1970**, *98*, 462–478. [CrossRef]
10. Jelesnianski, C.; Chen, J.; Shaffer, W.; Gilad, A. SLOSH-A hurricane storm surge forecast model. *OCEANS 1984* **1984**, *84*, 314–317. [CrossRef]
11. Luettich, R.A.; Westerink, J.J.; Scheffner, N.W.; ADCIRC: An Advanced Three-Dimensional Circulation Model for Shelves, Coasts, and Estuaries. Report 1, Theory and Methodology of ADCIRC-2DD1 and ADCIRC-3DL. 1992. Available online: https://apps.dtic.mil/sti/citations/ADA276150 (accessed on 15 March 2023).
12. Roelvink, J.; Van Banning, G. Design and development of DELFT3D and application to coastal morphodynamics. *Oceanogr. Lit. Rev.* **1995**, *11*, 925.
13. Blumberg, A.F.; Mellor, G.L. A description of a three-dimensional coastal ocean circulation model. *Three-Dimens. Coast. Ocean Model.* **1987**, *4*, 1–16. [CrossRef]
14. Chen, C.; Liu, H.; Beardsley, R.C. An unstructured grid, finite-volume, three-dimensional, primitive equations ocean model: Application to coastal ocean and estuaries. *J. Atmos. Ocean. Technol.* **2003**, *20*, 159–186. [CrossRef]
15. Weisberg, R.H.; Zheng, L. Hurricane Storm Surge Simulations for Tampa Bay. *Estuaries Coasts* **2006**, *29*, 899–913. [CrossRef]
16. Cuadra, C.; Suarez, J.K.; Biton, N.I.; Cabacaba, K.M.; Lapidez, J.P.; Santiago, J.; Mahar Francisco Lagmay, A.; Malano, V. Development of Inundation Map for Bantayan Island, Cebu Using Delft3D-Flow Storm Surge Simulations of Typhoon Haiyan. In Proceedings of the EGU General Assembly Conference Abstracts, Vienna, Austria, 27 April–2 May 2014; p. 15687.
17. Jisan, M.A.; Bao, S.; Pietrafesa, L.J. Ensemble projection of the sea level rise impact on storm surge and inundation at the coast of Bangladesh. *Nat. Hazards Earth Syst. Sci.* **2018**, *18*, 351–364. [CrossRef]
18. Chen, C.; Huang, H.; Lin, H.; Blanton, J.; Li, C.; Andrade, F. A Wet/Dry Point Treatment Method of FVCOM, Part II: Application to the Okatee/Colleton River in South Carolina. *J. Mar. Sci. Eng.* **2022**, *10*, 982. [CrossRef]
19. Wang, S.; Ge, J.; Kilbourne, K.H.; Wang, Z. Numerical simulation of mid-Holocene tidal regime and storm-tide inundation in the south Yangtze coastal plain, East China. *Mar. Geol.* **2020**, *423*, 106134. [CrossRef]
20. Li, M.; Zhang, F.; Barnes, S.; Wang, X. Assessing storm surge impacts on coastal inundation due to climate change: Case studies of Baltimore and Dorchester County in Maryland. *Nat. Hazards* **2020**, *103*, 2561–2588. [CrossRef]
21. Wang, K.; Hou, Y.; Li, S.; Du, M.; Li, R. Numerical Study of Storm Surge Inundation in the Southwestern Hangzhou Bay Region During Typhoon Chan-Hom in 2015. *J. Ocean Univ. China* **2020**, *19*, 263–271. [CrossRef]
22. Murty, P.L.N.; Rao, A.D.; Srinivas, K.S.; Rao, E.P.R.; Bhaskaran, P.K. Effect of Wave Radiation Stress in Storm Surge-Induced Inundation: A Case Study for the East Coast of India. *Pure Appl. Geophys.* **2019**, *177*, 2993–3012. [CrossRef]
23. Kowaleski, A.M.; Morss, R.E.; Ahijevych, D.; Fossell, K.R. Using a WRF-ADCIRC Ensemble and Track Clustering to Investigate Storm Surge Hazards and Inundation Scenarios Associated with Hurricane Irma. *Weather Forecast.* **2020**, *35*, 1289–1315. [CrossRef]

24. Wu, Z.; Chen, J.; Jiang, C.; Liu, X.; Deng, B.; Qu, K.; He, Z.; Xie, Z. Numerical investigation of Typhoon Kai-tak (1213) using a mesoscale coupled WRF-ROMS model—Part II: Wave effects. *Ocean Eng.* **2020**, *196*, 106805. [CrossRef]
25. Wu, Z.; Jiang, C.; Deng, B.; Chen, J.; Long, Y.; Qu, K.; Liu, X. Numerical investigation of Typhoon Kai-tak (1213) using a mesoscale coupled WRF-ROMS model. *Ocean Eng.* **2019**, *175*, 1–15. [CrossRef]
26. Thuy, N.B.; Tien, T.Q.; Wettre, C.; Hole, L.R. Monsoon-induced surge during high tides at the southeast coast of Vietnam: A numerical modeling study. *Geosciences* **2019**, *9*, 72. [CrossRef]
27. Ibarra, D.A.; Fennel, K.; Cullen, J.J. Coupling 3-D Eulerian bio-physics (ROMS) with individual-based shellfish ecophysiology (SHELL-E): A hybrid model for carrying capacity and environmental impacts of bivalve aquaculture. *Ecol. Model.* **2014**, *273*, 63–78. [CrossRef]
28. Dukhovskoy, D.S.; Morey, S.L.; Chassignet, E.P.; Chen, X.; Coles, V.J.; Cui, L.; Harris, C.K.; Hetland, R.; Hsu, T.-J.; Manning, A.J. Development of the CSOMIO coupled ocean-oil-sediment-biology model. *Front. Mar. Sci.* **2021**, *8*, 629299. [CrossRef]
29. Warner, J.C.; Armstrong, B.; He, R.; Zambon, J.B. Development of a coupled ocean–atmosphere–wave–sediment transport (COAWST) modeling system. *Ocean Model.* **2010**, *35*, 230–244. [CrossRef]
30. Holland, G.J. An analytic model of the wind and pressure profiles in hurricanes. *Mon. Weather Rev.* **1980**, *108*, 1212–1218. [CrossRef]
31. Shchepetkin, A.F.; McWilliams, J.C. The regional oceanic modeling system (ROMS): A split-explicit, free-surface, topography-following-coordinate oceanic model. *Ocean Model.* **2005**, *9*, 347–404. [CrossRef]
32. Haidvogel, D.B.; Arango, H.; Budgell, W.P.; Cornuelle, B.D.; Curchitser, E.; Di Lorenzo, E.; Fennel, K.; Geyer, W.R.; Hermann, A.J.; Lanerolle, L.; et al. Ocean forecasting in terrain-following coordinates: Formulation and skill assessment of the Regional Ocean Modeling System. *J. Comput. Phys.* **2008**, *227*, 3595–3624. [CrossRef]
33. Haidvogel, D.B.; Arango, H.G.; Hedstrom, K.; Beckmann, A.; Malanotte-Rizzoli, P.; Shchepetkin, A.F. Model evaluation experiments in the North Atlantic Basin: Simulations in nonlinear terrain-following coordinates. *Dyn. Atmos. Ocean.* **2000**, *32*, 239–281. [CrossRef]
34. Sun, J.; Li, J.; Ruan, Z.; Wu, K.; Li, F. Simulation study on the effect of atmosphere-ocean-wave interactions on Typhoon Rammasun (2014) in the South China Sea. *J. Atmos. Sol.-Terr. Phys.* **2021**, *212*, 105490–105503. [CrossRef]
35. Hegermiller, C.A.; Warner, J.C.; Olabarrieta, M.; Sherwood, C.R. Wave–current interaction between hurricane matthew wave fields and the gulf stream. *J. Phys. Oceanogr.* **2019**, *49*, 2883–2900. [CrossRef]
36. Liu, N.; Ling, T.; Wang, H.; Zhang, Y.; Gao, Z.; Wang, Y. Numerical simulation of Typhoon Muifa (2011) using a coupled ocean-atmosphere-wave-sediment transport (COAWST) modeling system. *J. Ocean Univ. China* **2015**, *14*, 199–209. [CrossRef]
37. Warner, J.C.; Defne, Z.; Haas, K.; Arango, H.G. A wetting and drying scheme for ROMS. *Comput. Geosci.* **2013**, *58*, 54–61. [CrossRef]
38. Schloemer, R.W. *Analysis and Synthesis of Hurricane Wind Patterns over Lake Okeechobee*; US Department of Commerce-Weather Bureau: Florida, USA, 1954.
39. Vickery, P.J.; Wadhera, D. Statistical Models of Holland Pressure Profile Parameter and Radius to Maximum Winds of Hurricanes from Flight-Level Pressure and H*Wind Data. *J. Appl. Meteorol. Climatol.* **2008**, *47*, 2497–2517. [CrossRef]
40. Powell, M.; Soukup, G.; Cocke, S.; Gulati, S.; Morisseau-Leroy, N.; Hamid, S.; Dorst, N.; Axe, L. State of Florida hurricane loss projection model: Atmospheric science component. *J. Wind Eng. Ind. Aerodyn.* **2005**, *93*, 651–674. [CrossRef]
41. Pan, Y.; Chen, Y.; Li, J.; Ding, X. Improvement of wind field hindcasts for tropical cyclones. *Water Sci. Eng.* **2016**, *9*, 58–66. [CrossRef]
42. Miyazaki, M. Theoretical investigations of typhoon surges along the Japanese coast. *Oceanogr. Mag.* **1961**, *13*, 51–75.
43. Pande, M.; Ho, T.; Mikitiuk, M.; Kopp, G.; Surry, D. Implications of Typhoon York on the design wind speeds in Hong Kong. *J. Wind Eng. Ind. Aerodyn.* **2002**, *90*, 1569–1583. [CrossRef]
44. Wang, X.; Yao, C.; Gao, G.; Jiang, H.; Xu, D.; Chen, G.; Zhang, Z. Simulating tropical cyclone waves in the East China Sea with an event-based, parametric-adjusted model. *J. Oceanogr.* **2020**, *76*, 439–457. [CrossRef]
45. Wei, K.; Shen, Z.; Wu, L.; Qin, S. Coupled Numerical Simulation on Wave and Storm Surge in the Coastal Areas under Strong Typhoon. *Eng. Mech.* **2019**, *36*, 139–146. (In Chinese) [CrossRef]
46. Vickery, P.J.; Masters, F.J.; Powell, M.D.; Wadhera, D. Hurricane hazard modeling: The past, present, and future. *J. Wind Eng. Ind. Aerodyn.* **2009**, *97*, 392–405. [CrossRef]
47. Marchesiello, P.; McWilliams, J.C.; Shchepetkin, A. Open boundary conditions for long-term integration of regional oceanic models. *Ocean Model.* **2001**, *3*, 1–20. [CrossRef]
48. Umlauf, L.; Burchard, H. A generic length-scale equation for geophysical turbulence models. *J. Mar. Res.* **2003**, *61*, 235–265. [CrossRef]
49. Zhang, K.; Liu, H.; Li, Y.; Xu, H.; Shen, J.; Rhome, J.; Smith, T.J., III. The role of mangroves in attenuating storm surges. *Estuar. Coast. Shelf Sci.* **2012**, *102*, 11–23. [CrossRef]
50. Warner, J.C.; Sherwood, C.R.; Signell, R.P.; Harris, C.K.; Arango, H.G. Development of a three-dimensional, regional, coupled wave, current, and sediment-transport model. *Comput. Geosci.* **2008**, *34*, 1284–1306. [CrossRef]
51. Egbert, G.D.; Erofeeva, S.Y. Efficient inverse modeling of barotropic ocean tides. *J. Atmos. Ocean. Technol.* **2002**, *19*, 183–204. [CrossRef]

52. Loveland, T.R.; Belward, A. The international geosphere biosphere programme data and information system global land cover data set (DISCover). *Acta Astronaut.* **1997**, *41*, 681–689. [CrossRef]
53. Nelli, N.R.; Temimi, M.; Fonseca, R.M.; Weston, M.J.; Thota, M.S.; Valappil, V.K.; Branch, O.; Wulfmeyer, V.; Wehbe, Y.; Al Hosary, T. Impact of roughness length on WRF simulated land-atmosphere interactions over a hyper-arid region. *Earth Space Sci.* **2020**, *7*, e2020EA001165. [CrossRef]
54. Feng, X.; Yin, B.; Yang, D.; William, P. The effect of wave-induced radiation stress on storm surge during Typhoon Saomai (2006). *Acta Oceanol. Sin.* **2011**, *30*, 20–26. [CrossRef]
55. Orton, P.; Georgas, N.; Blumberg, A.; Pullen, J. Detailed modeling of recent severe storm tides in estuaries of the New York City region. *J. Geophys. Res. Ocean.* **2012**, *117*, 1–17. [CrossRef]
56. Zhu, S.; Sha, W.; Ding, P.; Chen, X. An Asymmetry Wind Field Model of Typhoon near Shore. *J. East China Norm. Univ. (Nat. Sci.)* **2002**, *3*, 66–71. (In Chinese)
57. Zhu, J.; Ye, L.; Chen, D.; Li, Y.; Lin, Y. Numerical simulation of storm surge in Xiamen Bay and its adjacent seas caused by typhoon"Moranti"(1614). *Mar. Forecast.* **2020**, *37*, 20–30. (In Chinese)
58. Rey, W.; Mendoza, E.T.; Salles, P.; Zhang, K.; Teng, Y.-C.; Trejo-Rangel, M.A.; Franklin, G.L. Hurricane flood risk assessment for the Yucatan and Campeche State coastal area. *Nat. Hazards* **2019**, *96*, 1041–1065. [CrossRef]
59. Zachry, B.C.; Booth, W.J.; Rhome, J.R.; Sharon, T.M. A national view of storm surge risk and inundation. *Weather Clim. Soc.* **2015**, *7*, 109–117. [CrossRef]
60. Dean, R.G.; Walton, T.L. Wave setup. In *Handbook of Coastal and Ocean Engineering*; World Scientific: New Jersey, USA, 2010; pp. 1–23.
61. Stockdon, H.F.; Sallenger, A.H., Jr.; Holman, R.A.; Howd, P.A. A simple model for the spatially-variable coastal response to hurricanes. *Mar. Geol.* **2007**, *238*, 1–20. [CrossRef]
62. Chen, W.-B.; Chen, H.; Hsiao, S.-C.; Chang, C.-H.; Lin, L.-Y. Wind forcing effect on hindcasting of typhoon-driven extreme waves. *Ocean Eng.* **2019**, *188*, 106260. [CrossRef]
63. Rey, W.; Ruiz-Salcines, P.; Salles, P.; Urbano-Latorre, C.P.; Escobar-Olaya, G.; Osorio, A.F.; Ramírez, J.P.; Cabarcas-Mier, A.; Jigena-Antelo, B.; Appendini, C.M. Hurricane Flood Hazard Assessment for the Archipelago of San Andres, Providencia and Santa Catalina, Colombia. *Front. Mar. Sci.* **2021**, *8*, 766258. [CrossRef]
64. Rey, W.; Salles, P.; Torres-Freyermuth, A.; Ruíz-Salcines, P.; Teng, Y.-C.; Appendini, C.M.; Quintero-Ibáñez, J. Spatiotemporal storm impact on the northern Yucatan coast during hurricanes and central American cold surge events. *J. Mar. Sci. Eng.* **2019**, *8*, 2. [CrossRef]